ELSEVIER

International Journal of Heat and Fluid Flow 21 (2000) 664–673

International Journal of
HEAT AND
FLUID FLOW

www.elsevier.com/locate/ijhff

Large eddy simulation of the flow through the blades of a swirl generator

Stephen Conway [*], Doru Caraeni, Laszlo Fuchs

Division of Fluid Mechanics, Department of Heat and Power Engineering, Lund Institute of Technology, S-221 00 Lund, Sweden

Abstract

Subsonic turbulent flow between the blades of a swirl generator is considered using large eddy simulations (LES). The boundary layer exhibits transition in the upstream parts of the blade. Further downstream, the flow separates both on the suction and the pressure surfaces. In the boundary layer, one may note the streaky vortices. In addition, due to the blade surface curvature large, time-dependent streamwise vortices are formed. The wake of the blades also contains large scale, time-dependent structures. These phenomena are captured directly by LES. In our study, we use two different subgrid scale (SGS) models: the first model is an implicit model and the second is a novel dynamic model dubbed the dynamic divergence model (DDM). The effects of the SGS model and the grid resolution are also investigated. © 2000 Begell House Inc. Published by Elsevier Science Inc. All rights reserved.

Keywords: Large eddy simulation; Turbulence; Swirl generator

1. Introduction

Modern low NOx gas turbine burners often operate in the lean, premixed, prevaporised (LPP) mode. To carry out vaporisation and mixing in a limited space, a highly swirling flow is induced. The high levels of turbulence and large shearing rates associated with such swirling flows enhance the mixing process and provide a more homogeneous fuel–air mixture to the combustor. The role of the swirl generator is therefore of great importance for the overall performance of the gas turbine. Standard computations of the flow within LPP burners are often based on the Reynolds averaged Navier–Stokes (RANS) equations. Most often the classical k–ϵ model is used to account for the turbulence in the flow. Models of this type can be adequate if one is interested in obtaining a general view of the mean flow variables. However they, along with all eddy viscosity-based models, cannot account for many of the effects that determine the properties of the LPP burner. For instance, one may note that separation of the boundary layer on the burners' swirl generator blade surfaces and the shedding of low-frequency spanwise vortices occurs. The surface curvature of the blades also causes the formation of slowly varying streamwise vortices. These phenomena, in addition to the boundary layer streamwise streaks are important for the mixing and unsteadiness of the flow (and ultimately of the flame) in the burner. The unsteady separation of the boundary layer on both sides of the blade surface is synchronised with the previously mentioned coherent structures. As these effects are beyond the scope of eddy viscosity models and since we are interested in capturing the interaction of the boundary layer with the rest of the flow, we use the large eddy simulation (LES) approach in our studies.

The advent of the supercomputer has led to a marked increase in computing power and greatly reduced computational times. Now LES is becoming a real alternative to traditional turbulence models even for moderate Reynolds number engineering flows, (Fureby, 1998; Piomelli, 1998).

LES has been applied to flows in more complex geometries to a very limited extent. The major reasons for this are due to the need for describing the non-trivial geometry accurately whilst limiting the number of computational grid points. Additional difficulties occur due to grid non-uniformities and difficulties in achieving the higher order accuracy which is often claimed to be mandatory for LES. In addition, LES results can only be interpreted in terms of time-averages (i.e., after filtering out the high-frequency time fluctuations). Hence, the acquisition of the required amount of data for time averaging results in long computation times. These factors explain the difficulties in using LES for industrial problems on a routine basis. Modelling aspects of complex flows add to these difficulties. The flow may, as in the case studied here, be transitional and non-isotropic implying that subgrid scale (SGS) models with fixed model parameters are likely to be inapplicable. Dynamic SGS models in which the model parameters can be evaluated as part of the solution – their activation and deactivation being dependent on the local and instantaneous conditions – do not suffer from such limitations. We therefore propose the use of a new dynamic divergence model (DDM) in

---

[*] Corresponding author. Present address: The Aeronautical Research Institute of Sweden, Box 11021, SE-161 11 Bromma, Sweden. Tel.: +46-8-555-49437; fax: +46-8-555-49071.

E-mail address: stephen.conway@ffa.se (S. Conway).

PII: S0142-727X(00)00058-8

Notation

C	model parameter
C_f, C_{F}	skin friction coefficient
D	domain
f	frequency
G	generalised filter function
h	enthalpy
L	characteristic length
L_{ij}	resolved turbulent stress tensor
M_{ij}	dynamic scaling tensor
p	pressure
q	any variable
$\mathbf{R}$	residuals
S_{ij}	strain rate tensor
t	time
T	temperature
T_{ij}	subtest scale stress tensor
u_i	velocity component
U_{free}	freestream velocity
x_i	spatial coordinate
Greeks	
α_{ij}	parameterised subgrid scale stress tensor
β	coefficient in time discretisation scheme
β_{ij}	parameterised subtest scale stress tensor
γ	coefficient in time discretisation scheme
δ_{ij}	Kronecker delta
Δ	filter width
κ	thermal conductivity
μ_t	eddy viscosity
ν	kinematic viscosity
ρ	density
σ_{ij}	molecular stress tensor
τ	pseudo-time parameter
τ_{ij}	subgrid scale stress tensor
Φ	viscous dissipation

which three model parameters are evaluated independently, and thus naturally account for flow anisotropy. In previous papers, (Caraeni et al., 1999; Conway and Fuchs, 1997, 1998), we have established the basic properties of the used solvers and some initial results have been presented. Here, we describe the applicability of the LES method for yielding a deeper insight into the physical processes that take place in the swirl generator.

To evaluate different numerical aspects of the results we have considered two different spatial discretisation schemes, two computational grids with different resolutions and two SGS models. The effects of separation and transition are investigated. A vortex shedding frequency from the swirl generator blades is determined which is seen to be dependent on the angle of incident air flow. Interaction between the movement of the separation region and the shedding frequency is also noted. Such vortex shedding phenomena can directly affect the quality of fuel and air mixing within the combustion chamber and can in some cases induce vibrations in the gas turbine structure. Comparisons between the results obtained using different grid resolutions with an implicit model and the proposed DDM model are also made.

2. Large eddy simulation

In order to separate the large scales from the small scales, a spatial filtering operation is introduced. A generalised filter G applied to a variable q results in a filtered (space averaged) variable $\overline{q}$ according to

$$\bar{q}(x,t;\Delta)=\int_D \bar{G}(x-x';\Delta)\,q(x',t)\,\mathrm{d}x', \tag{1}$$

where Δ is the filter width, D the entire domain and $\bar{G}(x-x';\Delta)$ is the filter function which often has a compact support in LES. The discretisation process itself introduces a filtering of the unsupported frequency components of the function being approximated. Different explicit filters may also be introduced. The most common filters are the Fourier cutoff filter, the Gaussian filter and the top-hat filter. One may utilize the fact that the form of the filter function does not enter into the equations, with exception of the boundary conditions, where it slightly alters the boundary conditions, i.e., second-order correction in terms of the filter size, (Gullbrand et al., 1999). By choosing particular filters which have exact (differential) inverses one may derive an exact and explicit form for SGS terms (Fuchs, 1996).

Applying any of the filtering operations to the governing equations for a compressible flow gives, following Erlebacher et al. (1990):

$$\frac{\partial\bar{\rho}}{\partial t}+\frac{\partial\overline{\rho u_j}}{\partial x_j}=0, \tag{2}$$

$$\frac{\partial\overline{\rho u_i}}{\partial t}+\frac{\partial\overline{\rho u_i u_j}}{\partial x_j}=-\frac{\partial\bar{p}}{\partial x_i}+\frac{\partial\overline{\sigma_{ij}}}{\partial x_j}, \tag{3}$$

$$\frac{\partial\overline{\rho h}}{\partial t}+\frac{\partial\overline{\rho u_i h}}{\partial x_i}=\frac{\partial\bar{p}}{\partial t}+\overline{u_i\frac{\partial p}{\partial x_i}}+\frac{\partial}{\partial x_i}\left(\overline{\kappa\frac{\partial T}{\partial x_i}}\right)+\bar{\Phi}. \tag{4}$$

In this case, density averaging in space has been carried out in an analogous form to the time averaging of the RANS equations, e.g., the velocity field can be decomposed into: $u_i=\tilde{u}+u_i''$, where $\tilde{u}_i=\overline{\rho u_i}/\bar{\rho}$. In the momentum equation (Eq. (3)), the non-linear terms can be rearranged and written as

$$\tau_{ij}=-\bar{\rho}\left(\widetilde{u_i u_j}-\tilde{u}_i\tilde{u}_j\right), \tag{5}$$

where τ_{ij} is the SGS stress tensor. A similar rearrangement of the energy equation (Eq. (4)) gives rise to the SGS heat flux tensor. It is these SGS tensor relations which have to be modelled. The most common, and simplest explicit SGS model is that of Smagorinsky (1963). This model resembles Boussinesq's eddy viscosity hypothesis which is often used in the RANS framework

$$\tau_{ij}-\frac{1}{3}\tau_{kk}\delta_{ij}=2\mu_T\tilde{S}_{ij}. \tag{6}$$

Here $\tilde{S}_{ij}$ is the strain rate tensor of the filtered velocity

$$\tilde{S}_{ij}=\frac{1}{2}\left(\frac{\partial\tilde{u}_i}{\partial x_j}+\frac{\partial\tilde{u}_j}{\partial x_i}\right). \tag{7}$$

An algebraic model for the eddy viscosity μ_T can be derived from dimensional arguments to be

$$\mu_T=C\Delta^2|\tilde{S}|, \tag{8}$$

where C is the Smagorinsky model parameter, Δ the filter width (which in its simplest and most usual form is taken to be $\Delta=(\Delta_1\Delta_2\Delta_3)^{1/3}$, where Δ_i is the filter width associated with the filter in the ith coordinate direction) and $|\tilde{S}| = (2\tilde{S}_{ij}\tilde{S}_{ij})^{1/2}$. It has been found that the value of the Smagorinsky model parameter is not universal, but varying widely for different flow situations. It has also been found that in the presence of shear, near solid boundaries or in transitional flows the commonly used value is too large. The Smagorinsky model is also absolutely dissipative and does not allow for the intermittent transport of energy from the small scales to the large ones. This backscattering phenomenon is important when modelling transition. Piomelli et al. (1991) found that roughly half of the grid points in a DNS of transition were experiencing backscatter. A subgrid scale model which can account for backscatter is the scale similarity model of Bardina et al. (1980).

There also exists another group of SGS models known as dynamic SGS models. Dynamic models, first introduced by Germano et al. (1991), advance the scale similarity concept one stage further, namely that the smallest resolved scale motions and the largest subgrid scale motions are similar in structure. In such models, the model coefficients are calculated dynamically from the resolved flow field as the computation progresses. The model introduced by Germano is based on two filters. In addition to the grid filter, which is commonly used in the first filtering operation, a second test filter, whose width $\hat{\Delta}$ is larger than the base filter (Δ), is used:

$$\widehat{\bar{q}}(x,t;\Delta) = \int_D \widetilde{G}\left(x - x';\hat{\Delta}\right)\bar{q}\left(x',t\right)\,\mathrm{d}x'. \tag{9}$$

As with the stress tensor terms which appear when the grid filter is applied to the Navier–Stokes equations, the test filter defines a new set of stresses, known as the subtest scale stresses T_{ij}:

$$T_{ij} = -\bar{\rho}\left(\widehat{\widetilde{u_i u_j}} - \widehat{\tilde{u}}_i\,\widehat{\tilde{u}}_j\right). \tag{10}$$

The subtest scale stresses and the subgrid scale stresses are related to each other by the resolved turbulent stresses, L_{ij}, which can be expressed using Germano's identity (Germano, 1992), as

$$L_{ij} = T_{ij} - \hat{\tau}_{ij} = -\widehat{\bar{\rho}}\left(\widehat{\tilde{u}_i\tilde{u}_j} - \widehat{\tilde{u}}_i\,\widehat{\tilde{u}}_j\right). \tag{11}$$

Parameterising the subgrid and subtest scale stresses with an eddy viscosity model (most commonly the Smagorinsky model) gives

$$\tau_{ij} - \frac{1}{3}\delta_{ij}\tau_{kk} = -2C\Delta^2|\tilde{S}|\tilde{S}_{ij} = -2C\alpha_{ij}, \tag{12}$$

and

$$T_{ij} - \frac{1}{3}\delta_{ij}T_{kk} = -2C\hat{\Delta}^2|\widehat{\tilde{S}}|\widehat{\tilde{S}}_{ij} = -2C\beta_{ij}. \tag{13}$$

Substituting Eqs. (12) and (13) into Eq. (11) gives an expression for L_{ij} in terms of the modelled quantities

$$L_{ij} = C\beta_{ij} - \widehat{C\alpha_{ij}}. \tag{14}$$

The tensor relation for L_{ij} was initially solved by Germano et al. by contraction with the mean rate of strain $\tilde{S}_{ij}$. An additional assumption was that the model parameter was a slowly varying function in space, allowing it to be moved outside of the test filter. The algebraic equation for the model parameter thus becomes

$$C = \frac{L_{ij}\tilde{S}_{ij}}{M_{kl}\tilde{S}_{kl}}, \tag{15}$$

where

$$M_{ij} = \beta_{ij} - \hat{\alpha}_{ij}. \tag{16}$$

A potential problem with this expression is the fact that the denominator can and does become zero, making C indeterminate or ill-conditioned. Germano and co-workers avoided this by averaging in homogeneous directions. Further modification by Lilly (1991) using a least-square method to reduce the error in computing the single coefficient C resulted in the following equation:

$$C = \frac{L_{ij}M_{ij}}{M_{kl}M_{kl}}. \tag{17}$$

The denominator in this case is always positive. The relation may however give rise to highly negative values of the coefficient which can result in numerical instability. Olsson and Fuchs (1996, 1998) used artificial bounding of the model parameter to limit the negative values and have shown that relatively small regions are affected by the limitations. Based on this method the following artificial bounds have been used in this work:

$$C^{(i)} \leqslant C_{\max} = \frac{0.5\nu}{LU_{\text{free}}}, \tag{18}$$

and

$$C^{(i)} \geqslant C_{\min} = \frac{-0.01\nu}{LU_{\text{free}}}, \tag{19}$$

where L is a characteristic length of the flow, ν the kinematic viscosity and U_{free} is the freestream velocity.

This dynamic model requires determining six model coefficients. In many cases, a single coefficient is used. However, by recognising that in the momentum equations one uses only the divergence of the SGS stress tensor, three independent expressions for the three remaining model parameters can be derived. Following Held and Fuchs (1997) the DDM can be derived as follows:

$$L_{ij,j} = T_{ij,j} - \hat{\tau}_{ij,j} = -\left(\widehat{\bar{\rho}}\,\widehat{\tilde{u}_i\tilde{u}_j} - \widehat{\bar{\rho}}\,\widehat{\tilde{u}}_i\,\widehat{\tilde{u}}_j\right)_{,j}, \tag{20}$$

where the divergence of the subgrid scale stress and the subtest stress are modelled using the Smagorinsky model for compressible flows

$$\tau_{ij,j} = C^{(i)}\left(2\Delta^2\bar{\rho}|\tilde{S}|\left(\tilde{S}_{ij} - \frac{1}{3}\hat{S}_{kk}\delta_{ij}\right)\right)_{,j} = C^{(i)}\alpha_{ij,j}, \tag{21}$$

and

$$T_{ij,j} = C^{(i)}\left(2\hat{\Delta}^2\widehat{\bar{\rho}}|\widehat{\tilde{S}}|\left(\widehat{\tilde{S}}_{ij} - \frac{1}{3}\widehat{\tilde{S}}_{kk}\delta_{ij}\right)\right)_{,j} = C^{(i)}\beta_{ij,j}. \tag{22}$$

Note that no summation over superscript (i) is performed. The three model parameters are calculated during the simulation, one for each coordinate direction by combining Eqs. (20)–(22)

$$C^{(i)} = \frac{L_{ij,j}}{\beta_{ik,k} - \hat{\alpha}_{il,l}}. \tag{23}$$

In this way, the model is able to allow for the effects of anisotropy in the turbulent flow.

3. Numerical methods

Since the SGS term is of second-order in terms of the filter, one may argue that in order to distinguish between the truncation errors and the SGS contribution one should use higher than second-order discrete approximations. One may also argue that the behaviour of the SGS term is $\mathrm{O}(\Delta^{4/3})$ (Moin et al., 1994). The basis for the latter estimate is that the turbulent dissipation rate is determined by the SGS model and the net supply rate of the turbulent kinetic energy from larger to small scales. Thus, the numerical dissipation scale, i.e., the numerical Kolmogorov scale, is proportional to the filter size (Δ). This implies that the total viscosity behaves as the Kolmogorov scale to the power of 4/3. Therefore, the total effect of viscous dissipation implies a contribution of $O(\Delta^{4/3})$ in the momentum equations. With this estimate, one could argue that any discretisation of order greater than two would allow one to discriminate between the physical and numerical contribution to the SGS behaviour. Supporting evidence for this is that second-order central differences applied to the flow past a cylinder produce better velocity power spectra, as compared to experiments, than high-order upwind schemes. The lower order statistics appear to be comparable, Moin (1998). The arguments concerning the order of discretisation schemes are only correct for fluctuations that are well resolved. For fluctuations with scales close to the grid size, estimates based on Taylor expansions are questionable.

For more complex geometries one has to use non-uniform grids. Higher than second-order discretisations require explicit and accurate data on the properties of the grid. Such discretisations also use larger stencils and tend to result in spatial oscillations and slower convergence. Hence, the most commonly used spatial discretisation schemes for complex geometries are of second-order. In our study, we have considered two such schemes in two different solvers. The first solver uses a cell-centred finite volume scheme for structured meshes with second- and fourth-order artificial dissipation terms (Jameson et al., 1981). The second solver uses a spatial discretisation scheme based on the so-called “fluctuation splitting” of Deconinck et al. (1994) for unstructured tetrahedral meshes.

Both schemes use implicit time stepping for time discretisation. For the structured solver, the discretisation process can be described as follows. Consider a general three-level implicit discretisation:

$$\frac{\beta_1\mathbf{q}^{n+1}+\beta_0\mathbf{q}^n+\beta_{-1}\mathbf{q}^{n-1}}{\Delta x}+\gamma_1\mathbf{R}(\mathbf{q}^{n+1})+\gamma_0\mathbf{R}(\mathbf{q}^n)+\gamma_{-1}\mathbf{R}(\mathbf{q}^{n-1})=0, \tag{24}$$

where $\mathbf{q}$ are the unknowns, $\mathbf{R}$ the residuals and the γ and β coefficients are chosen to give the desired accuracy and stability. In this case, a backward difference scheme was used and hence the coefficients, obtained from a Taylor expansion around $\mathbf{q}^{n+1}$, were

$$\beta_1=\frac{3}{2},\quad \beta_0=-2,\quad \beta_{-1}=\frac{1}{2},\quad \gamma_1=1,\quad \gamma_0=0,\quad \gamma_{-1}=0. \tag{25}$$

To avoid time consuming factorisation methods normally used in implicit schemes the governing equations are reformulated to yield a steady-state problem at each implicit time step. The steady-state problem can be described by introducing the pseudo-time, τ and denoting the dependent variables $\mathbf{q}^{n+1}$ by $\mathbf{q}^*(\tau)$, hence

$$\frac{\mathrm{d}\mathbf{q}^*}{\mathrm{d}\tau}+\mathbf{R}^*(\mathbf{q}^*)=0, \tag{26}$$

where

$$\mathbf{R}^*(\mathbf{q}^*)=\frac{\beta_1\mathbf{q}^*}{\Delta t}+\gamma_1\mathbf{R}(\mathbf{q}^*)+\mathbf{Q} \tag{27}$$

and

$$\mathbf{Q}=\frac{\beta_0\mathbf{q}^n+\beta_{-1}\mathbf{q}^{n-1}}{\Delta t}+\gamma_0\mathbf{R}(\mathbf{q}^n)+\gamma_{-1}\mathbf{R}(\mathbf{q}^{n-1}) \tag{28}$$

is a constant source term. As steady state in pseudo-time is approached

$$\frac{\mathrm{d}\mathbf{q}^*}{\mathrm{d}\tau}\to 0\Rightarrow \mathbf{q}^*\to\mathbf{q}^{n+1}. \tag{29}$$

Within each time step, the set of differential equations given by Eq. (26) are solved using an explicit four-stage Runge–Kutta method. The time discretisation procedure is described in more detail in Eliasson and Nordström (1995).

4. Results

4.1. Computed cases

We consider the flow through a swirl generator. Two versions of the swirl generator geometry are considered. In the first version, depicted in Fig. 1, a simplified swirl generator is considered in which the correct shape of the swirl generator blades is used but it is assumed that the blades have uniform span and are infinite. Blocked structured grids are used to define this geometry. In the second version, the true topology of the swirl generator is considered and is defined using unstructured tetrahedral grids. The study limits itself to the study of the air flow through the swirl generator at low temperature. An ideal gas approximation is adopted. Unless otherwise stated, the results shown are related to the simplified geometry. It is interesting to note however that the basic phenomena and frequencies found in the simulations with the full geometry can also be observed in the results obtained from the simplified geometry.

The airflow between the upper surface of one blade and the lower surface of the next blade in the swirl generator cascade is considered. Periodic boundary conditions are applied in the normal blade direction to enable the modelling of the effect the blade cascade has on the flow. A similar boundary condition is also used in the spanwise direction. Riemann invariants are used as both the inflow and outflow boundary conditions and no slip conditions are applied to the blade surface. The Reynolds number based on the blade chordlength is 100,000 and the inlet Mach number is 0.3. The series of simulations include calculations with the blade tilted at angles of 0° and 15° with respect to the freestream velocity, calculations using two different SGS models and calculations using two different grid resolutions, see Table 1. An implicit SGS model and the DDM model described previously are used. In the implicit model, the SGS terms are modelled through the numerical truncation error. Numerical viscosity dissipates energy and in this sense

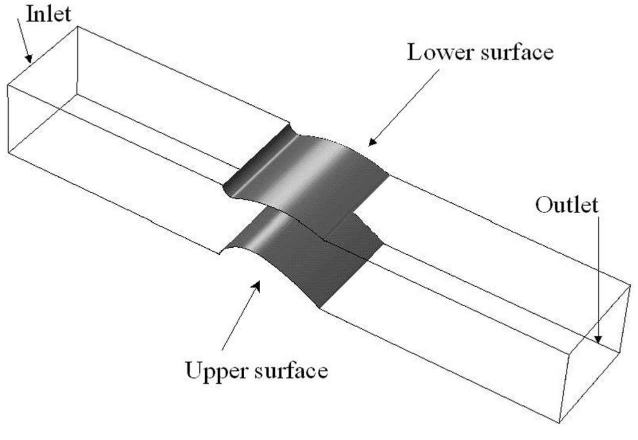

Fig. 1. Simplified swirl generator geometry.

Table 1
Computed cases

Grid	SGS model	Blade angle
Coarse	DDM, Implicit	0°, 15°
Fine	DDM, Implict	0°

acts like an SGS model. The computational grids used were a coarse grid of roughly 80,000 cells and a finer grid of roughly 225,000 cells for the simpler geometry and a grid of roughly 250,000 cells for the full geometry. In all cases, grid stretching in the normal direction enabled good resolution of the flow close to the surface of the blade. Similar grid stretching in the freestream direction enabled most of the cells to be positioned around the blade surface.

4.2. Resolution

An estimate of the spatial resolution of the computational grid can be obtained by plotting the energy spectrum of turbulent kinetic energy as a function of frequency. Sampling data from a point in the wake and comparing the resulting spectra for different grid resolutions and different SGS models with Kolmogorov's $-5/3$ decay shows the effect these have on the resolution, Fig. 2. As expected higher frequencies are supported when the mesh is refined. It can also be seen that the fine mesh computation using the DDM gives the best agreement with Kolmogorov's $-5/3$ decay. In LES the smallest scales are not fully resolved, but are instead modelled by the SGS term. The "knee" in the energy spectrum can be seen as a cutoff point between the resolved and unresolved scales, and hence a measure of spatial resolution. Wavenumbers above this cutoff point are not supported by the grid. In the case of the coarse mesh this is seen at roughly $\log(f) = 2.9$ and for the fine mesh at roughly $\log(f) = 3.1$.

4.3. Flow instabilities and transition

Although the underlying mechanisms of transition are still not fully understood, being able to predict when transition will occur and in some cases aiding the onset of it and turbulence can be of great benefit in a wide range of industrial applications. The occurrence of transition is readily obtainable from LES data. By considering Fig. 3, which depicts iso-contours of vorticity on the upper blade surface, and Fig. 4, which depicts iso-surfaces of vorticity located between the blades, one can observe the transition from an initially laminar flow to a turbulent flow as the vortices stretch and deform. At the leading edge of the blade, a laminar-attached boundary layer region is formed. Further along the blade, the boundary layer separates and the iso-contours and iso-surfaces become more non-uniform as the vortices become stretched and deformed.

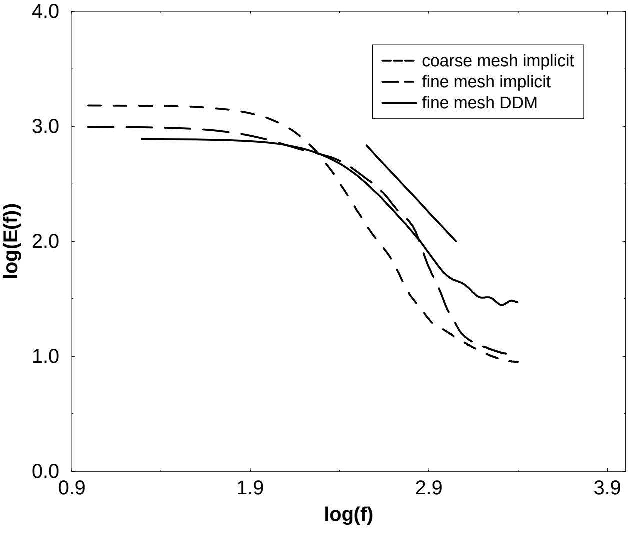

Fig. 2. Energy spectrum at a point in the wake for two grid resolutions, the implicit and the DDM SGS models.

The point of separation of the boundary layer can be obtained from skin friction data on the surface of the blade. Fig. 5 shows the variation in mean skin friction coefficient, $\overline{C}_F$ with chordlength on both surfaces at both blade angles. In this plot, C_F is averaged in both time and the spanwise direction.

The point where the skin friction becomes negative defines the mean point of separation. On the upper surface, the skin friction becomes negative at roughly 30% chordlength for both blade angles. This value is comparable with the region in which vortex stretching is first noticed in Fig. 3. After this point, the flow remains separated and a large area of recirculation is present. The vortices produced in the separated boundary layer

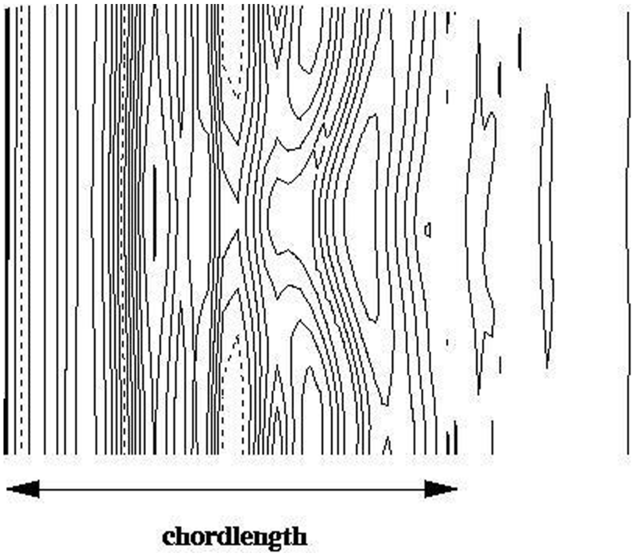

Fig. 3. Iso-contours of vorticity on the upper blade surface.

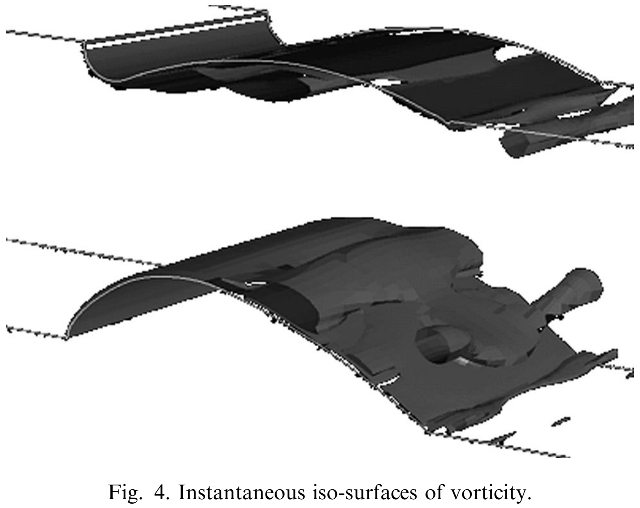

Fig. 4. Instantaneous iso-surfaces of vorticity.

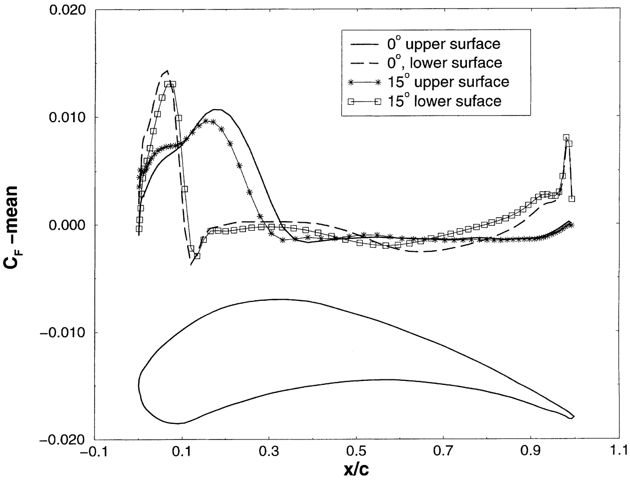

Fig. 5. Mean skin friction coefficient for 0° and 15° cases on both blade surfaces.

are convected downstream. On the lower surface, separation occurs much earlier at between 10% and 15% chordlengths. The frequency with which the vortices are shed from the upper surface of the blade can be obtained by taking a fast Fourier transform of the velocity at discrete points in the domain over a period of time. Fig. 6 shows the shedding frequency at two points on the upper surface of the blade and at two points in the wake for the 0° case. From these plots it can be clearly seen that a low-frequency vortex of roughly 125 Hz is shed and travels into the wake. The intensity of the vortex decreases as it travels further downstream, the effect of such vortices on the fuel–air mixing process within the gas turbine can be significant. They are also a probable explanation for the mechanical vibrations which can occur under certain operating conditions. Increasing the blade incidence angle to 15° results in a change in the shedding frequency. Fig. 7 shows that in this case a shedding frequency of roughly 110 Hz is produced. The amplitude of the vortices is seen to increase and is almost double that of the 0° case.

Blade angle is also seen to have an influence on the mean point of separation. As can be seen in Fig. 5, in the 15° case the point of separation occurs slightly nearer the trailing edge on the upper surface than in the 0° case. On the lower surface the flow remains attached slightly longer, separating at roughly 15% chordlength.

The RMS of the skin friction coefficient fluctuations is shown in Fig. 8 for both the 0° and 15° cases. The intensity of the fluctuations increases on the lower surface after separation. At this stage, the fluctuations on the lower surface are more intensive than on the upper surface due to the fact that the flow on the upper surface does not separate until much later. The intensity of skin friction fluctuations on the upper surface increases greatly in the turbulent boundary layer, and from 50% chordlength the fluctuations on the upper surface are more pronounced than on the lower surface. The large increase in the fluctuations on the lower surface is probably due to flow acceleration in this region.

By computing the instantaneous skin friction, one can follow the time-dependent separation and reattachments. From the gathered data, an accurate measure of the mean point of separation can be obtained. In the 0° case, the mean point of separation on the upper surface occurs at 30% chordlength and in the 15° case at 28% chordlength. More important, however, is the effect the time-dependent separation has on the boundary layer and on vortex shedding. In the 0° case, it was noted that a dominant frequency was shed from the upper surface into the wake at 125 Hz. Taking a fast Fourier transform of the time-dependent separation data results in the frequencies shown in Fig. 9. In the 0° case (a) it is notable that dominant frequencies of roughly 40 and 125 Hz are produced. For the 15° case (b), dominant frequencies are apparent at roughly 25, 50 and 110 Hz. This indicates that the frequency of vortex shedding is directly affected by the movement of the point of

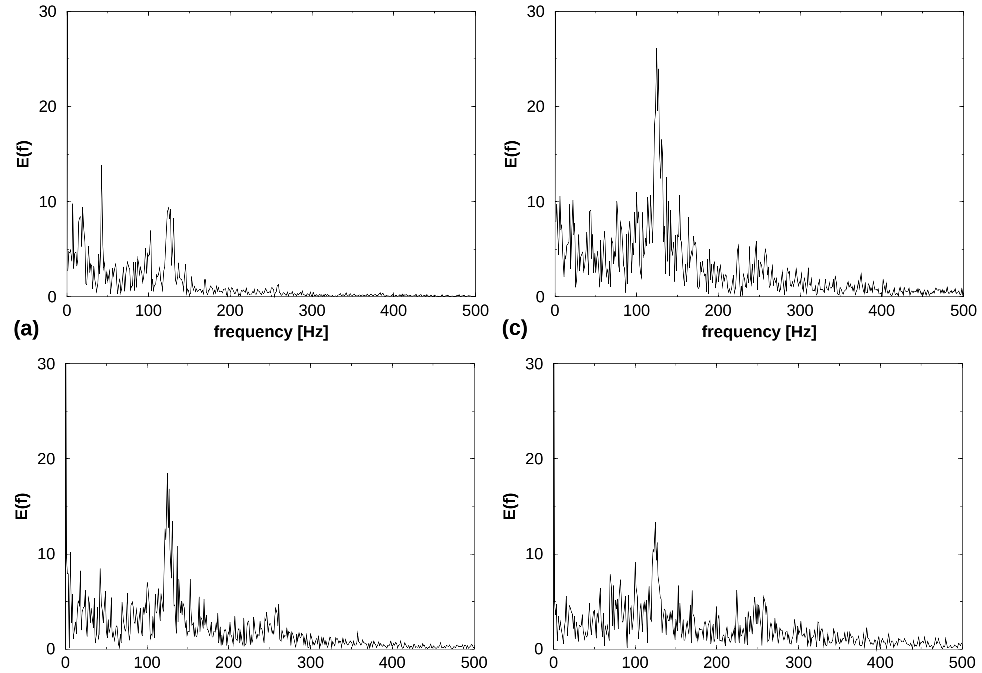

Fig. 6. Shedding frequency for the 0° case at (a) 90% and (b) 99% chordlength and in (c) wake and (d) far wake.

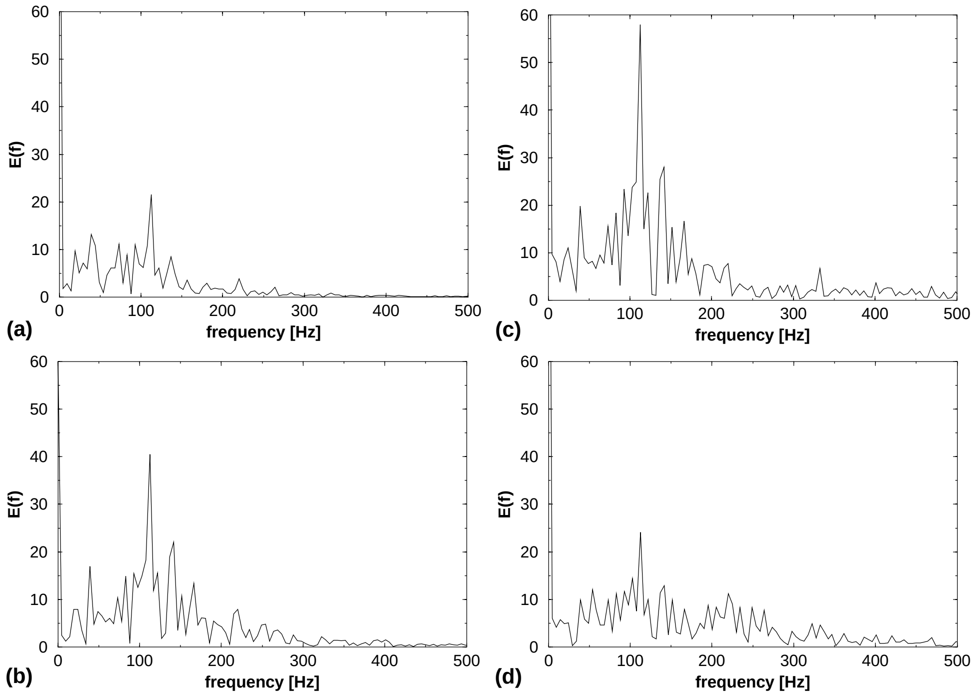

Fig. 7. Shedding frequency for the 15° case at (a) 90% and (b) 99% chordlength and in (c) wake and (d) far wake.

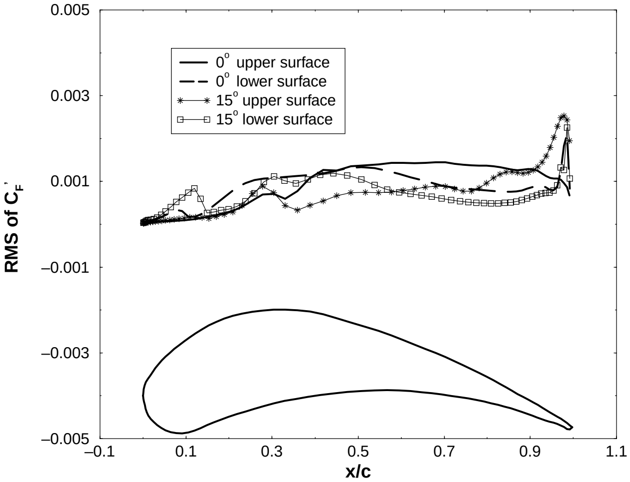

Fig. 8. RMS of skin friction coefficient fluctuations for 0° and 15° cases on both blade surfaces.

separation, and that the dominant frequencies of 125 and 110 Hz obtained at the trailing edge and in the wake in the respective cases are harmonics of the low-frequency vortex found further upstream.

The energy content of the fundamental frequency is very low and its influence is seen to diminish rapidly as the trailing edge is approached. As an example of this, Fig. 10 shows the energy spectrum at different points on the upper surface of the blade for the 0° case. Initially at the leading edge, two peaks at 45 and 125 Hz are prominent. Further downstream, the energy content of these frequencies has increased but is still very low. The energy content of the 45 Hz peak diminishes greatly after 80% chordlength and the influence of the 125 Hz peak increases greatly as shown previously in Fig. 6.

The effects of the finite size blades with variable chordlength can be obtained from the computations carried out on the full swirl generator geometry, and can be assessed by comparing the mean and the fluctuating root mean square values of the skin friction. Fig. 11 depicts the mean skin friction on the pressure side of the blade, where a large, non-uniform separation bubble can be noticed. It stretches from the root of the blade, where the separation bubble extends to over 90% of the blade surface, towards the tip. The separation bubble disappears at about 80% of the blade height measured from the root. The level of fluctuations in the skin friction is very large near the root of the blade and parallel to its leading edge. The levels of fluctuations on the skin friction are smallest in the central parts of the blade.

The stretching of vortices plays a vital role in transition to turbulence. Fig. 12 shows an instantaneous velocity field between the upper and lower blade surfaces. Large regions of separated flow are apparent on both surfaces. As seen in Fig. 3, separation is closely related to the regions of deforming vortices.

The streamwise vortices generated between the blades can be seen more clearly in Fig. 13, which depicts the projection of instantaneous velocity at a plane normal to the blade surface at roughly 30% chordlength. The streamwise vortices are generated by centrifugal instabilities due to the concavity of the blade. The instability governing the formation of these streamwise-oriented, counter-rotating vortices, more commonly known as Görtler vortices, obeys Rayleigh's circulation criterion, i.e., that the inability of the local pressure gradient to restrain an excess in angular momentum of a particle undergoing an outward virtual displacement leads to instability, (Saric, 1994). The Görtler instability is known to be an important factor in the transition to turbulence and the vortex structures existence in blade passages is widely accepted. The increase in the skin friction coefficient fluctuations after separation on the lower surface, described previously and shown in Fig. 8, is a direct result of the increased vorticity.

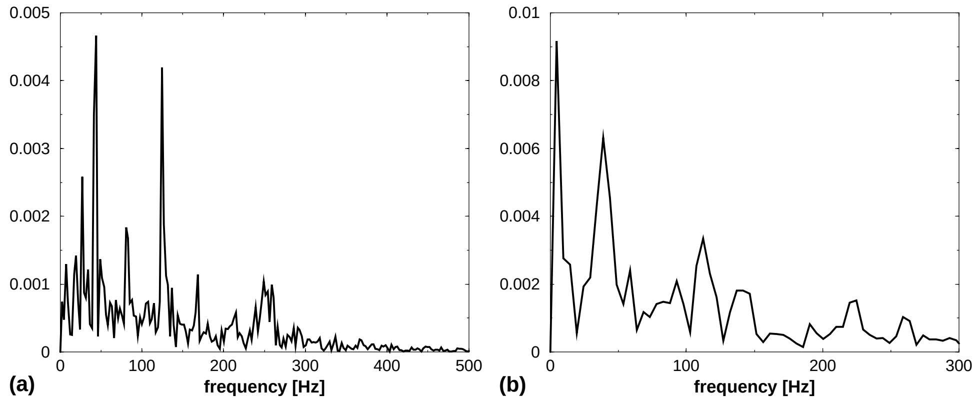

Fig. 9. Frequency of point of separation on the upper blade surface for (a) 0° and (b) 15°.

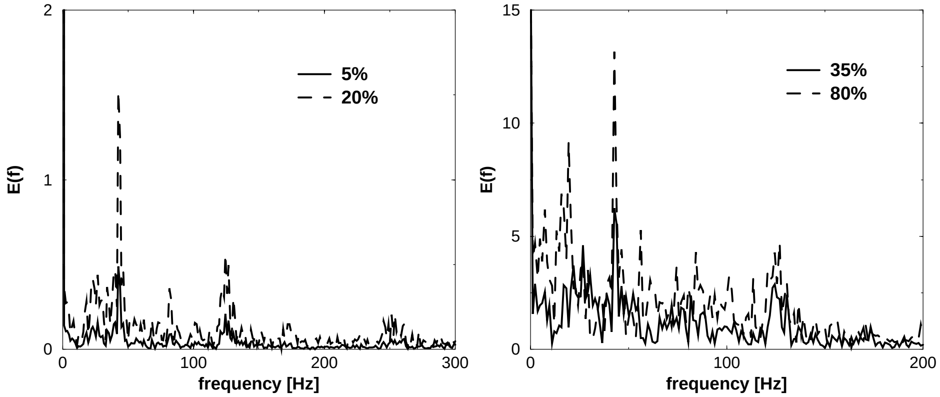

Fig. 10. Energy spectra at four points on the upper blade surface.

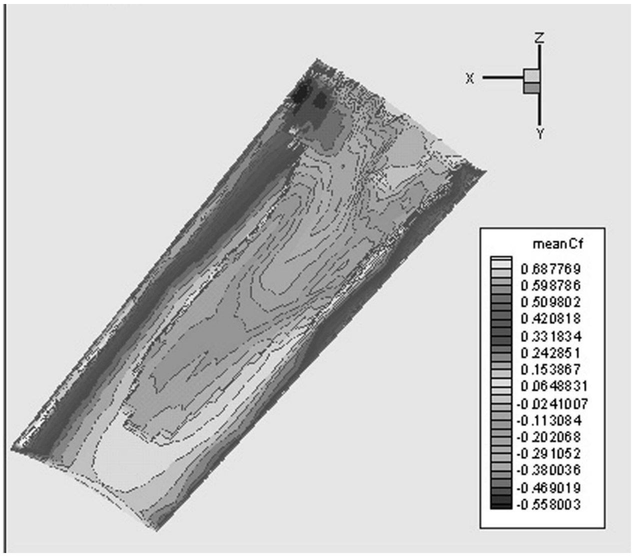

Fig. 11. Mean skin friction coefficient on the upper surface for the full three-dimensional geometry.

4.4. Model and grid effects

To be able to make comparison between different SGS models and different grids, a statistically stationary mean field is necessary. The mean values were obtained by averaging the instantaneous values measured at a point in the wake over approximately 4000 time steps. This number of time steps turned out to be adequate for determining the mean of the dependent variables rather accurately. Two different SGS models have been used in this investigation on two different grid resolutions. The first model is a model where the SGS terms are modelled implicitly by the numerical truncation

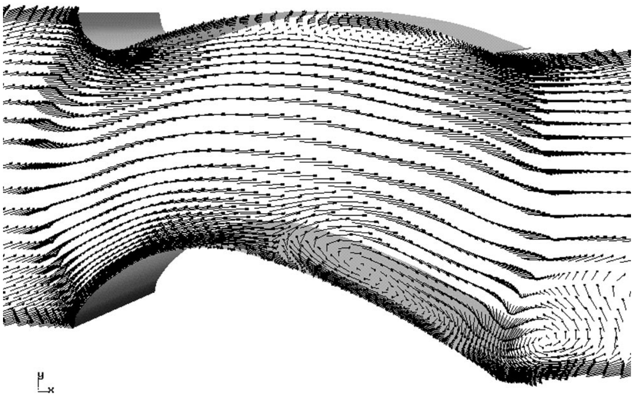

Fig. 12. Instantaneous velocity field showing large regions of separated flow.

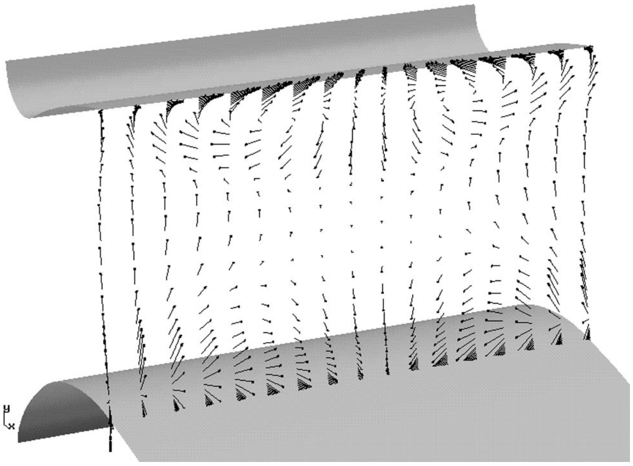

Fig. 13. Instantaneous velocity field at a cross-sectional plane located at 30% chordlength.

error. The second model is the DDM model described previously.

As was shown in Fig. 2, the use of a finer mesh leads to an increase in the spatial resolution and the introduction of an explicit SGS model leads to better agreement with Kolmogorov's $-5/3$ decay. In Fig. 14, a comparison between the mean skin friction coefficient on the blade surfaces is made. On the upper surface there is very little difference in the computed values. Both the implicit and DDM model produce a large region of separated flow from approximately 30% chordlength. A larger difference in skin friction is obtained however on the lower surface. Here a 60% difference in mean skin friction is obtained at roughly 10% chordlength.

The construction of the DDM model is such that it is only active in regions of transition and turbulence. Although it can allow for intermittent backscatter from the small to the large scales, an overall energy transport from the large scales to the small scales is apparent and essential. By comparing the intensity of skin friction coefficient fluctuations, we can gain some idea of the influence of the SGS models on the flow. Fig. 15 shows the RMS of the skin friction coefficient fluctuations on both blade surfaces. Slight variations in intensity are apparent with the implicit model giving higher intensities. This is possibly due to the restrictions placed on the DDM model parameters. Further investigations are however required before any conclusion can be drawn on this matter.

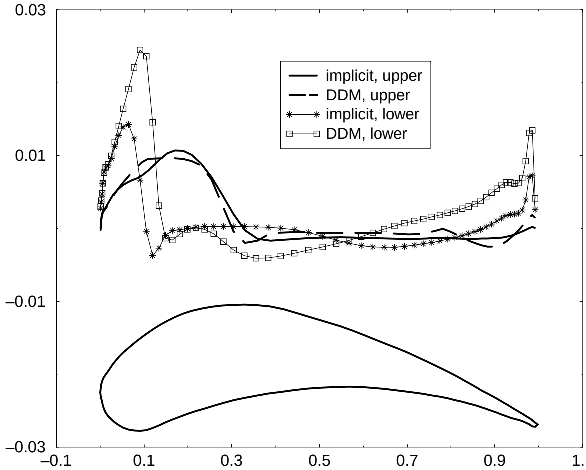

Fig. 14. Mean skin friction coefficient for 0° case on both blade surfaces computed using implicit and DDM SGS models.

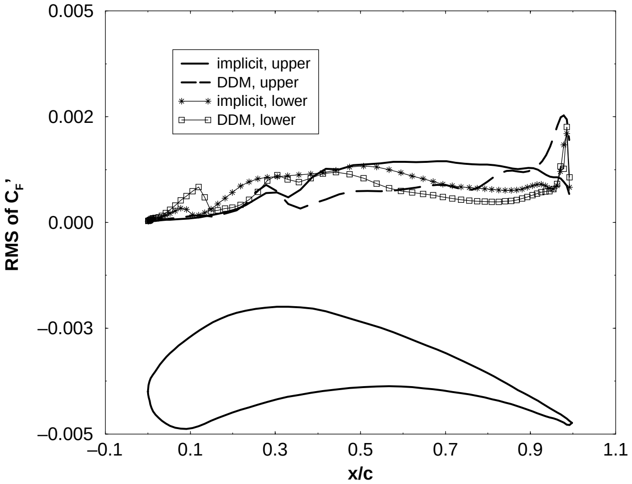

Fig. 15. RMS of skin friction coefficient fluctuations for 0° case on both blade surfaces computed using implicit and DDM SGS models.

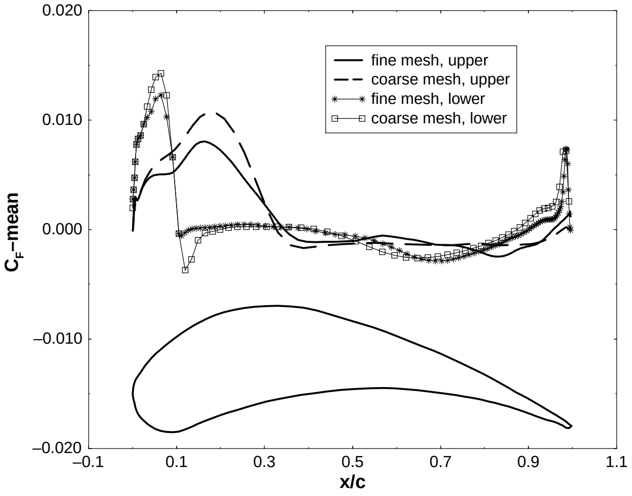

Fig. 16. Mean skin friction coefficient for 0° case on both blade surfaces for the coarse and fine meshes.

Only a limited amount of time steps were performed on the fine mesh. It is therefore difficult to make comparisons with higher order statistical values. Instead, low-order statistics calculated from mean values are considered. The time required to obtain mean properties is much shorter than that required to obtain higher order statistics. Fig. 16 shows the mean skin friction results for the 0° case on the upper blade surface obtained using the implicit SGS model. The mean point of separation occurs at roughly the same position for both meshes. The length of the separation region is also seen to be very similar. Higher mean skin friction values are obtained in regions of high-speed flow for the coarse mesh simulation on both the upper and lower surfaces.

5. Concluding remarks

In this study, we have applied the LES technique to the moderate Reynolds number flow through a swirl generator using two different geometries and two SGS models. The use of LES has allowed the study of many interesting flow details. The presence of transition, time-dependent separated regions, spanwise and streamwise time-dependent vortices, together with vortex shedding downstream of the blades left no other modelling alternative. The results enabled us to relate the shedding frequency to the frequency of the separated boundary layer. It was observed that the angle of incidence of the blade to the freestream flow affected the shedding frequency which is an important parameter if one is to avoid structural vibrations. By refining the computational grid and comparing an implicit and dynamic DDM SGS model, we found that grid refinement had a similar effect to the introduction of the SGS model. The SGS model acts primarily to compensate for the interaction between the nearly unresolved with the nearly resolved scales.

Acknowledgements

This work was sponsored by Sydkraft AB, via the Research Centre for Combustion Processes at Lund Institute of Technology. We are also grateful to The Centre for Scientific and Technical Computing at Lund University, LUNARC for providing computing resources.

References

Bardina, J., Ferziger, J.H., Reynolds, W.C., 1980. Improved subgrid scale models for large eddy simulation. AIAA Paper 80-0825.

Caraeni, D., Conway, S., Fuchs, L., 1999. LES of the flow in a bladed diffuser. In: Banerjee, Eaton (Eds.), Turbulence and Shear Flow-1. Begell House Inc., pp. 759–765.

Conway, S., Fuchs, L., 1997. Large eddy simulation of the flow across a swirl generator. In: Taylor, C. (Ed.), Numerical Methods in Laminar and Turbulent flows X. Pineridge, Swansea, pp. 823–834.

Conway, S., Fuchs, L., 1998. Investigation of the flow across a swirl generator using LES. AIAA Paper 98-0921.

Deconinck, H., Struijs, R., Bourgois, G., Roe, P.L., 1994. High resolution shock capturing cell vertex advection schemes on unstructured grids. VKI Lecture Series.

Eliasson, P., Nordström, J., 1995. The development of an unsteady solver for moving meshes. FFA TN 1995-39.

Erlebacher, G., Hussaini, M.Y., Speziale, C.G., Zang, T.A., 1990. Toward the large-eddy simulation of compressible turbulent flows. ICASE Report 90-76.

Fuchs, L., 1996. An exact SGS-model for LES. In: Proceedings of the Sixth European Turbulence Conference. Kluwer Academic Publishers, Dordrecht, pp. 55–62.

Fureby, C., 1998. Towards large eddy simulations of flows in complex geometries. AIAA Paper 98-2806.

Germano, M., Piomelli, U., Moin, P., Cabot, W.H., 1991. A dynamic subgrid-scale eddy viscosity model. Phys. Fluids A 3, 1760.

Germano, M., 1992. Turbulence: the filtering approach. J. Fluid. Mech. 238, 325–336.

Gullbrand, J., Revstedt, J., Fuchs, L., 1999. A comparison of subgrid scale models for large eddy simulation of a co-annular swirling flow field. In: S. Banerjee, J.K. Eaton (Eds.), Turbulence and Shear Flow 1, Begell House, pp. 747–752.

Held, J., Fuchs, L., 1997. Large eddy simulation of compressible separated flow around a NACA 0012 wing section. AIAA Paper 97-1931.

Jameson, A., Schmidt, W., Turkel, E., 1981. Numerical solutions of the Euler equations by finite volume methods using Runge–Kutta time-stepping schemes. AIAA Paper 81-1259.

Lilly, D.K., 1991. A proposed modification of the Germano subgrid-scale closure method. Phys. Fluids A 4, 633.

Moin, P., Carati, D., Lund, T., Ghosal, S., Akselvoll, K., 1994. Development and application of dynamic models for LES of complex flows. AGARD CP-551.

Moin, P., 1998. Numerical and physical issues in large eddy simulation of turbulent flows. JSME Int. J. Series B 41, 454–463.

Olsson, M., Fuchs, L., 1996. Large eddy simulation of the proximal region of a spatially developing circular jet. Phys. Fluids 8, 2125.

Olsson, M., Fuchs, L., 1998. Large eddy simulation of a forced semi-confined circular impinging jet. Phys. Fluids 10, 476.

Piomelli, U., Cabot, W., Moin, P., Lee, S.L., 1991. Subgrid-scale backscatter in turbulent and transitional flows. Phys. Fluids A 3, 1766.

Piomelli, U., 1998. Large eddy simulations: present state and future directions. AIAA Paper 98-0534.

Saric, W.S., 1994. Görtler vortices. Annu. Rev. Fluid Mech. 26, 379.

Smagorinsky, J., 1963. General circulation experiments with the primitive equations. Mon. Weather Rev. 91, 99.